TEMPERATURE DISTORTION IN AN S-DUCT WITH INLET ICING AND HEAT TRANSFER

Jin, W.*, Taghavi, R. R., and Farokhi, S.
*Author for correspondence
Department of Aerospace Engineering,
University of Kansas,
Lawrence, KS 66045,
USA,
E-mail: jwonjin@ku.edu

ABSTRACT

An S-duct inlet used in aircraft gas turbine engines is computationally studied for the effects of inlet icing and wall heat transfer. A Reynolds-Averaged Navier-Stokes (RANS) code with k-ω turbulence model is used to simulate the compressible viscous flow in the duct. Engine face distortion is analyzed with particular emphasis on the static temperature distortion. The glaze-ice accretion on the inlet lip, which can significantly impact engine face distortion, is modeled using the numerical icing shape. Inlet lip separation, increased internal blockage, and internal shocks do appear in the S-duct as a result of glaze-inlet icing at freestream Mach numbers of 0.475 and 0.85. The additional flow separation that is induced by the shock-boundary layer interaction due to the inlet icing creates a stronger secondary flow pattern at the engine face. The wall thermal boundary condition for zero heat transfer and the heated wall boundary condition allow for the simulation of realistic temperature distortion at the engine face under inlet icing conditions. Stall margin deterioration as a result of both total pressure and static temperature distortion is presented.

NOMENCLATURE

DC	[~]	Total pressure distortion coefficient, defined in equation 2
DP	[~]	Total pressure distortion parameter, defined in equation 1
D	[m]	Diameter
LWC	[g/m³]	Liquid water content
MVD	[μm]	Mean volume diameter of water droplet
M	[~]	Mach number
p	[kPa]	Pressure
q	[kPa]	Dynamic pressure
T	[K or °R]	Static temperature
TD	[~]	Static temperature distortion, defined in equation 4
Tu_∞	[~]	Freestream turbulence level
ΔT	[K or °R]	Static temperature increment
$\Delta T_{ef,\,max}$	[K or °R]	Maximum static temperature distortion at the engine face, defined in equation 3
x, y, z	[~]	Cartesian coordinates

Greek Symbols
θ	[deg]	Angle in cylindrical coordinates

Superscript
$^{-A}$	Area averaged

Subscripts
ef	Engine face
max	Maximum
min	Minimum
t	Total
th	Inlet throat
w	Wall
∞	Freestream

INTRODUCTION

The air intake system for aircraft gas turbine engines, in buried configurations, uses S-duct, double curvature geometry. A simple curved duct induces a *secondary flow* pattern, which in the case of an S-duct; it is further amplified and azimuthally rotates in the second bend. A *diffusing* S-duct, which is suitable for an aircraft inlet system, has an additional burden of potential flow separation due to the streamwise adverse pressure gradient in the diffuser. These, i.e., the combined flow separation and secondary flow pattern, contribute to the problem of engine face distortion. The level of *distortion* that an inlet creates at the compressor face affects the performance and the stability of the compressor and engine performance. Distortion represents non-uniformity in the flow. The non-uniformity in total pressure as in boundary layers, wakes and free shear layers, the non-uniformity in temperature as in gun gas ingestion or thrust reverser flow ingestion, or wall heating with inlet icing, and the non-uniformity in density, as created by hot gas ingestion and wall heat transfer are some of the different types of distortion. The penalty associated with all different types of distortion is their destabilization effect on the compressor performance and the cyclic loads they impose on compressor blades. This means that all types of distortions reduce the stability margin of a compressor or fan, potentially to the level of compressor stall or the engine surge.

However, the most frequently encountered inlet distortion in flight is due to total pressure that is caused by separated boundary layers in the inlet. If the boundary layer management system in a supersonic inlet, as in the bleed

system, fails to react to an abrupt change in the flight operation, the flowfield at the engine face will contain large *patches* of low-energy, low momentum flow that could cause flow separation in the front stage(s) of the fan or compressor, as in rotating stall, or even a breakdown of the entire flow in the compressor, known as surge. Povolny, *et al.* [1] simulated four distortion patterns at the compressor face using a J-85 turbojet engine. The four types of simulated inlet-total pressure distortion are shown in Figure 1 (from Farokhi [2]). They found that the order of the least to the most impact on the stall margin deterioration, are: 1) radial hub, 2) radial tip, 3) circumferential hub, and 4) full-span circumferential distortion, respectively. Further research identified a critical circumferential extent of the spoiled sector that caused the maximum loss in the stall pressure ratio of a compressor is at nearly 60° [1]. This result, i.e., the critical extent, is of importance since the angular extent of distortion patches impacts the stability of the compression system.

The temperature distortion also leads to a reduction in stall margin. In practice, static temperature distortion in a flow brings about density distortion, which in turn creates a non-uniform velocity field. Consequently, it is impossible to create a static temperature distortion without creating other forms of non-uniformity, e.g., density, velocity, total pressure, and angularity in the flow. To quantify the impact of a spatial temperature distortion on engine stall behaviour, NASA researchers have conducted experiments with representative data shown in Figure 2 (from Povolny *et al.*[1]). The undistorted operating line, stall limit and different shaft speeds are shown in dashed lines. Data points corresponding to the effect of temperature distortions of ΔT=45-120 °F (i.e., 25 – 66.7 °C) on the stall behavior of a variable-geometry turbofan engine high-pressure compressor are plotted in solid lines. The circumferential extents of the temperature distortions were between 90 and 100 degrees in different tests. A ΔT=100 °F (i.e., 55.6 °C) distortion of β ~90°-100° circumferential extent is seen to stall the high-pressure compressor operating at its 90% corrected flow. For additional discussions on the impact of inlet distortion on compressor stall see Farokhi [2], or Seddon, *et al.* [3].
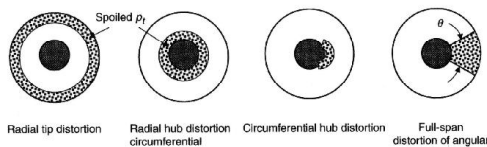

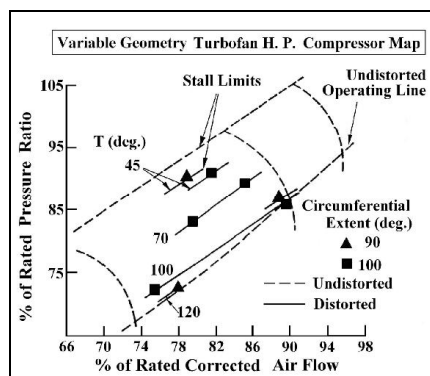**Figure 1** Total pressure distortion patterns (from Farokhi [2])

Figure 2 Impact of spatial temperature distortion on compressor stall (from Povolny *et al.* [1])

INLET ICING

The aircraft flying through clouds of super-cooled water droplets are always subject to ice accretion on its surfaces. Numerous experimental and numerical studies have been carried out for icing effect on the performance of airfoils and wings [4-8]. However, less attention has been paid to the icing effects on the performance of engine inlets, even though the effects are hazardous to engine stability and aircraft. In particular, ice accretion on the aircraft inlet lip can dramatically alter the shape of the inlet lip and cause serious degradation of the performance of an engine inlet duct. The air stream temperature and speed, liquid water content (LWC in g/m³) and the mean-volume diameter (MVD in *µm*) of water droplets impact the ice accretion and the icing shape. The two dominant forms of ice accretion shapes are *rime* and *glaze* and are shown in Figure 3 (from Henry, *et al.* [9]). As compared to rime ice accretion shape, glaze shape was found to contribute more to performance degradation due to its obstructive (horn) shape, according to Jin and Taghavi [10]. As a result, in this study, the effect of glaze ice accretion on the steady state flowfield inside a well-studied diffusing S-duct (i.e., M2129) inlet with two freestream Mach numbers of 0.475 and 0.85 are computationally investigated. The inlet is axisymmetric and the two bends in the S-duct are in-plane.
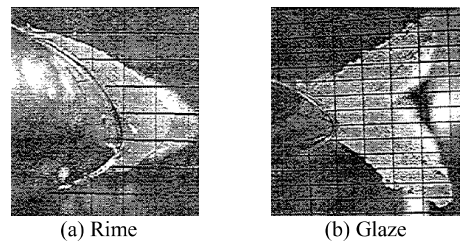

(a) Rime   (b) Glaze

Figure 3 Two dominant forms of leading edge icing shapes (from Henry, *et al.* [9])

NUMERICAL METHOD

The CFD code used for the viscous compressible flow simulation in the present study is Star-CCM+ [11]. The code is based on a finite volume method for the Reynolds-Averaged Navier Stokes (RANS) equations and uses a coupled-implicit solver. From a variety of turbulence models, we conducted a validation study with experimental data [12] and concluded that the Shear Stress Transport (SST) *k*-ω model produced the best match with the data for the baseline S-duct inlet (clean inlet). The use of *k*-ω turbulence modelling in diffusers with vortex separation and compressible flow in transonic diffusers is also supported by other researchers [13-15]. Validation of the computational results with the WIND-US code results [16] for the flowfields in the baseline M2129 S-duct inlet was also conducted. Grid sensitivity study on the performance of the M2129 S-duct was performed. Furthermore, as indicated by Anderson and Farokhi [17], the study on the near wall grid resolution showed that the CFD prediction with the smaller value of y⁺ produced relatively better results in the region of separation and the engine face of an M2129 S-duct inlet. Therefore, the value of y⁺ was set to be about 0.6 for the clean inlet, and y⁺ = 0.2 for the iced inlet case at the highest Mach number region inside the duct. Based on the numerical ice shape [18] defined by LEWICE3D code, the shape of glaze ice was simulated on the inlet lip of the M2129 S-duct inlet as shown in Figure 4. Structured grid generations for the clean and

glaze iced inlet lips, S-duct (Figure 5), and farfield boundary were performed using GAMBIT software [19]. The farfield boundary was radially extended by $20D_{th}$ into x-, y-, and z-directions upstream to prevent the farfield boundary effects on the simulation regions of interest. The number of grid nodes in the duct section was $230 \times 160 \times 100$ in the axial, circumferential, and radial direction. Therefore, the total number of the grid cells for all parts including the farfield region was approximately 5,200,000. All simulations were performed on the computing cluster at the Information and Telecommunication Technology Center (ITTC) at the University of Kansas. Total 96 Intel[®] Xeon[®] EM64T processors were dedicated for all simulations and each node has 4,096 MB memory. The calculations were continued and monitored until the residuals for continuity-, momentum-, energy-equation, and turbulence factors dropped below 10^{-4} where the magnitudes of the area-averaged total pressure at the engine face station are changed by less than 0.5 % between runs. The heated wall boundary condition was simulated through a constant wall temperature, T_w=350 K.
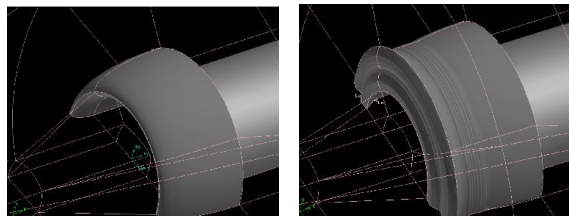

(a) Clean inlet lip   (b) Glaze iced inlet lip
**Figure 4** 3-D modelling of clean and glaze iced inlet lips
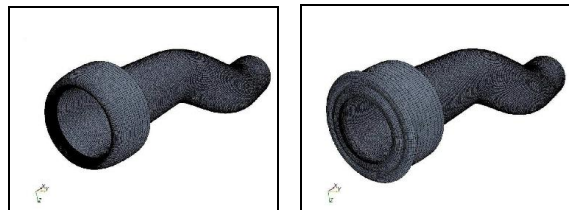
(a) Clean   (b) Glaze
Figure 5 Structured grid generations for inlet lip and S-duct inlet in GAMBIT [19]

COMPUTATIONAL RESULTS

The total pressure distribution in the plane of symmetry for the cases of *clean* and *glaze* at freestream Mach number of 0.475 is shown in Figure 6. Boundary layer separation is visible in both clean and glaze cases. However, the extent of the separation is significantly increased in the inlet with glaze ice. Figures 7 and 8 show the Mach number and static temperature contours, respectively, at the plane of symmetry for a clean inlet and the glaze ice accretion shape at freestream Mach number of 0.475. The Mach contours show a massive separation in the glaze case that starts at the convex corner of the first bend, which does not occur in the clean case. The temperature contour in the glaze case shows a similarly massive region in the duct separated flow that exhibits a higher temperature than the clean case. The engine face static temperature contours are shown in Figure 9. Temperature distortion is severe in the glaze case, as compared to the clean inlet, due to massive flow separation that we had noted earlier (Figures 6-8).
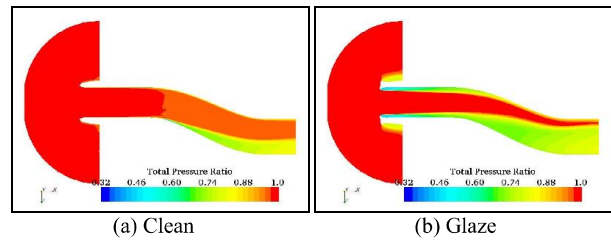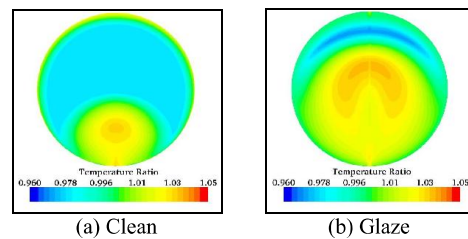

(a) Clean   (b) Glaze
Figure 6 Total pressure ratio ($p_t/p_{t\infty}$) distributions at the plane of symmetry ($p_{t\infty}$= 101.1 kPa, M_∞= 0.475)
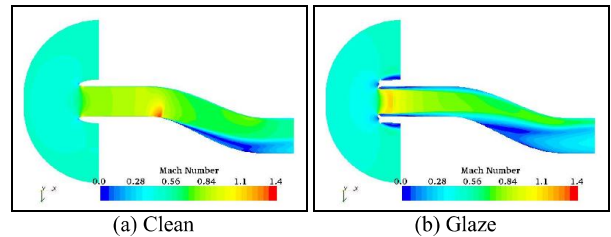
(a) Clean   (b) Glaze
Figure 7 Mach number distributions at the plane of symmetry ($p_{t\infty}$= 101.1 kPa, M_∞= 0.475)
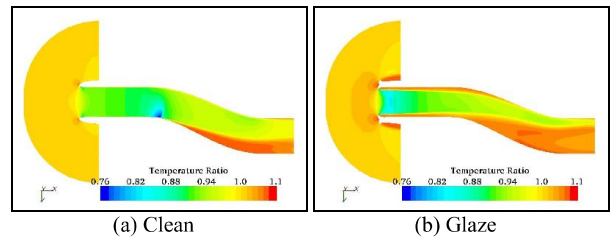
(a) Clean   (b) Glaze
Figure 8 Static temperature ratio (T/T_∞) distributions at the plane of symmetry (T_∞= 255 K, M_∞= 0.475)

(a) Clean   (b) Glaze
Figure 9 Static temperature ratio (T/T_∞) distributions at the engine face (T_∞= 255 K, M_∞ = 0.475)

The effect of higher flight Mach number, namely M_∞=0.85, on distortion levels are shown in Figures 10-13. The total pressure contours in Figure 10 show massive flow separation and subsequent lower total pressure recovery ($p_{tef}/p_{t\infty}$) in the glaze ice case as compared to the clean inlet. The effect of higher flight Mach number is seen in the appearance of shocks in the duct with subsequent boundary layer separation. Hence, the engine face distortion level is exacerbated by higher flight Mach number. The Mach distribution in the plane of symmetry is shown in Figure 11. Here, the intersecting oblique shocks and their multiple reflections from the wall are visible in the glaze ice case. The shock cell structure starts at the throat and multiple cells persist into the first and second bends of the S-duct. The static temperature profile at the plane of symmetry is shown in Figure 12. The static temperature distortion is dominated by the shocks and massive flow separation in the duct. The clean case shows a large separation zone at the top of the duct (θ=0°) whereas the glaze ice case shows a massive flow separation on the bottom, i.e., θ=180°. Therefore the engine

face temperature distortion follows the separated zones in the two cases, as shown in Figure 13. The effect of flight Mach number on engine face temperature distortion, for a clean inlet, is shown in Figure 14. Two separated zones on top and bottom of the (clean) S-duct at M_∞=0.85 versus a single separation at the bottom (θ=180°) for M_∞=0.475 are the dominant sources of temperature non-uniformity at the engine face. Therefore, higher flight Mach number exacerbates temperature distortion at the engine face, primarily due to the appearance of the shocks in the duct and flow separation topology. The effect of the flight Mach number on temperature distribution at the engine face in a glazed ice inlet is shown in Figure 15. Here we note that the lower flight Mach number (M_∞=0.475) has created a smoother temperature profile at the engine face than the case of M_∞=0.85, where repeated shock cells appeared in the duct and flow separations at the engine face became massive. As a result, temperature distortion is much more pronounced in the glazed ice case with higher flight Mach number.
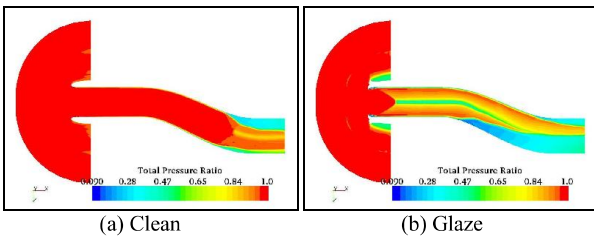

| (a) Clean | (b) Glaze |

Figure 10 Total pressure ratio ($p_t/p_{t\infty}$) distributions at the plane of symmetry ($p_{t\infty}$= 101.1 kPa, M_∞= 0.85)
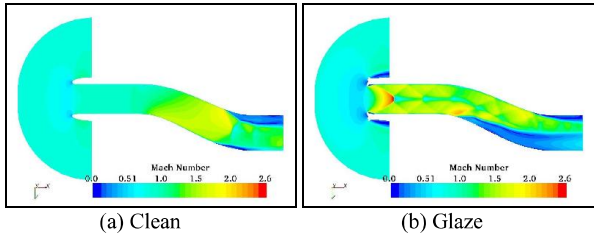

| (a) Clean | (b) Glaze |

Figure 11 Mach number distributions at the plane of symmetry ($p_{t\infty}$= 101.1 kPa, M_∞= 0.85)

| (a) Clean | (b) Glaze |
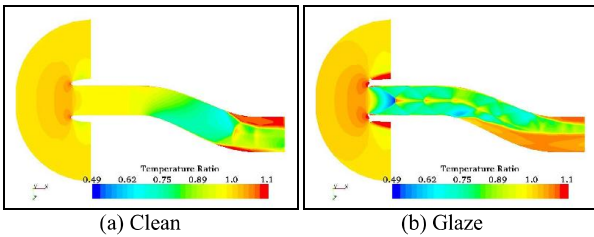
Figure 12 Static temperature ratio (T/T_∞) distributions at the plane of symmetry (T_∞= 233 K, M_∞= 0.85)

| (a) Clean | (b) Glaze |
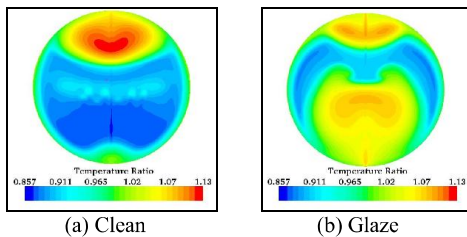
Figure 13 Static temperature ratio (T/T_∞) distributions at the engine face (T_∞= 233 K, M_∞= 0.85)

| (a) T_∞= 255 K, M_∞= 0.475 | (b) T_∞= 233 K, M_∞= 0.85 |
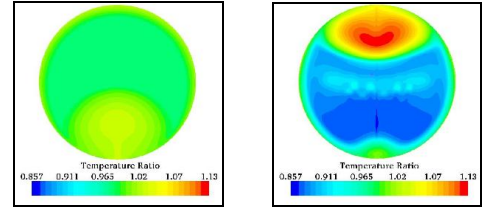
Figure 14 Static temperature ratio (T/T_∞) distributions at the engine face (clean)

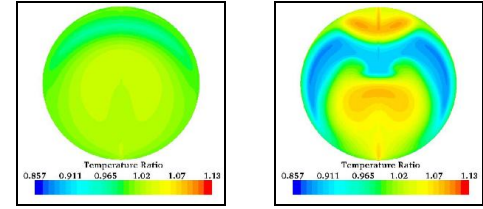| (a) T_∞= 255 K, M_∞= 0.475 | (b) T_∞= 233 K, M_∞= 0.85 |

Figure 15 Static temperature ratio (T/T_∞) distributions at the engine face (glaze)

To simulate a heated wall and the study of engine face distortion, we considered a constant wall temperature of T_w=350 K. The *area-averaged* engine face parameters, for a clean inlet, at two flight Mach numbers are summarized in Table 1. The case of glazed ice is summarized in Table 2. First, we note in the glaze case that the (area-averaged) total pressure is reduced with the heated wall at both low and high flight Mach numbers. Also, the mass flow rate drops about 2.5% for the glazed ice inlet at flight Mach number of 0.85 with the heated wall boundary condition. The reduced mass flow rate corresponds to lower densities in the flow when the wall is heated, as expected.

Table 1 Changes in area-averaged properties at the engine face with adiabatic and heated wall (clean)

(a) M_∞ = 0.475

Flowfield Properties	Adiabatic wall	T_W =350 K	Increment (%)
Total pressure (kPa)	95.751	95.654	-0.11
Static pressure (kPa)	80.217	79.941	-0.34
Static temperature (K)	253.58	257.41	1.51
Mach No.	0.50	0.50	0.68
Mass flow rate (kg/s)	22.45	22.39	-0.27

(b) M_∞ = 0.85

Flowfield Properties	Adiabatic wall	T_W =350 K	Increment (%)
Total pressure (kPa)	79.770	80.034	0.33
Static pressure (kPa)	37.325	37.517	0.52
Static temperature (K)	215.54	220.83	2.45
Mach No.	1.05	1.04	-0.70
Mass flow rate (kg/s)	22.49	22.40	-0.44

Table 2 Changes in area-averaged properties at the engine face with adiabatic and heated wall (glaze)

(a) M_∞ = 0.475

Flowfield Properties	Adiabatic wall	T_W =350 K	Increment (%)
Total pressure (kPa)	84.497	84.379	-0.14
Static pressure (kPa)	76.319	76.021	-0.39
Static temperature (K)	258.87	265.46	2.55
Mach No.	0.37	0.37	1.08
Mass flow rate (kg/s)	15.10	15.03	-0.42

(b) $M_\infty = 0.85$

Flowfield Properties	Adiabatic wall	$T_W = 350$ K	Increment (%)
Total pressure (kPa)	61.726	61.415	-0.51
Static pressure (kPa)	38.562	38.081	-1.25
Static temperature (K)	232.15	239.35	3.10
Mach No.	0.76	0.76	-0.04
Mass flow rate (kg/s)	17.05	16.61	-2.54

The total pressure distortion at the engine face with adiabatic and heated wall boundary conditions for a flight Mach number of 0.85 for a clean inlet is shown in Figure 16. The impact of heated wall is seen to be small for the clean inlet. Temperature distortion is more pronounced with heated wall, as shown in Figure 17. Here we note a more vivid separation of cold versus hot zones in the clean inlet case with heated wall. The glaze ice results for total pressure contours at the engine face are shown in Figure 18. The total pressure distortion (on top of the duct) is larger and more pronounced with wall heating, as closer examination of Figure 18 reveals. Similar behaviour is observed for the temperature distortion at the engine face, where higher gradients and larger islands of low and high temperature zones are produced in the heated wall case.
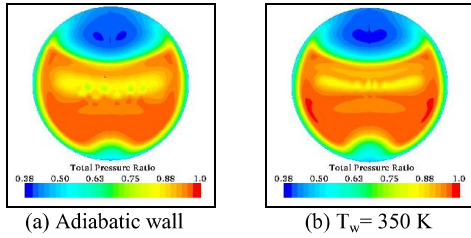

(a) Adiabatic wall   (b) $T_w = 350$ K

Figure 16 Total pressure distortions at the engine face with adiabatic and heated wall boundary conditions (clean, $M_\infty = 0.85$)
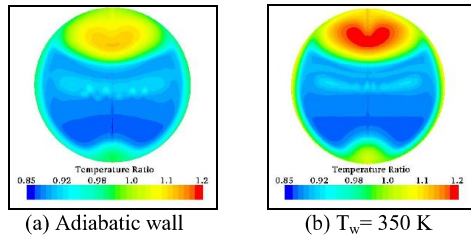

(a) Adiabatic wall   (b) $T_w = 350$ K

Figure 17 Static temperature distortions at the engine face with adiabatic and heated wall boundary conditions (clean, $M_\infty = 0.85$)
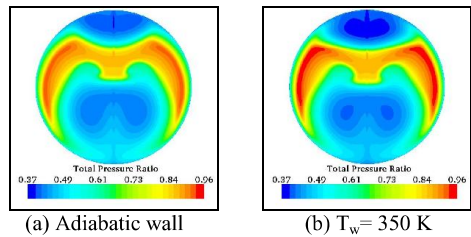

(a) Adiabatic wall   (b) $T_w = 350$ K

Figure 18 Total pressure distortions at the engine face with adiabatic and heated wall boundary conditions (Glaze, $M_\infty = 0.85$)

The amplitude of static temperature distortion at the engine face, ΔT_{ef}, is also a critical parameter, as evidenced in NASA engine tests (see Figure 2). We will examine this temperature distortion amplitude in a glaze ice accretion case with adiabatic and heated wall. To quantify the distortion at the engine face, we define and examine two distortion parameters for total pressure as:

$$DP \equiv \frac{p_{t,max} - p_{t,min}}{\bar{p}_t^A} \tag{1}$$

$$DC(\theta) \equiv \frac{\bar{p}_t^A - p_t(\theta)}{\bar{q}^A} \tag{2}$$

where DP denotes distortion parameter, and DC(θ) is distortion coefficient, $p_{t,\,max}$ and $p_{t,\,min}$ are maximum and minimum total pressures at the engine face respectively, $\bar{p}_t^A$ is the area-averaged total pressure (at the engine face) and $p_t(\theta)$ is the lowest area-average total pressure in a sector of θ extent. The first parameter highlights the maximum distortion, whereas the second parameter accounts for a critical sector impact on distortion and compressor stability. The angular extent of the spoiled sector, as noted in Figure 1, is taken to be $\theta = 60^o$ or higher. Subsequently, the distortion coefficient, so calculated, is denoted by DC(60). We also define a maximum temperature distortion parameter as signified by the difference between the highest and the lowest temperatures, $\Delta T_{ef,max}$ and a non-dimensional temperature distortion parameter, TD, at the engine face as:

$$\Delta T_{ef,\,max} = T_{ef,\,max} - T_{ef,\,min} \tag{3}$$

$$TD \equiv \frac{T_{ef,max} - T_{ef,min}}{\bar{T}_{ef}^A} \tag{4}$$

The non-dimensional distortion parameters for the cases of clean and glazed ice are summarized in Tables 3 and 4. A clean S-duct inlet at flight Mach number of 0.85 shows a total pressure recovery ($p_{tef}/p_{t\infty}$) of 78.8% (adiabatic wall). The same flight condition for a glazed ice inlet gives 61.04% total pressure recovery. This significant drop in performance is due to the glaze ice horns, flow blockage due to boundary layer separation, reflected shock cells, and massive flow separation in the S-duct. Now, let's examine the effect of heated wall in both clean and glazed ice inlet. The total pressure recovery is increased to 79.14% for the clean and reduced to 60.73% in the glaze ice case at $M_\infty = 0.85$. It seems that wall heating has energized some low-energy patches and thus caused a slightly higher total pressure recovery in the clean inlet. In the case of the glazed ice inlet, we note a reduced total pressure recovery, which indicates that wall heating leads to higher distortion. This effect may also be seen DC(60) and DP parameters. The temperature distortion, TD, shows a significant rise in heated wall case, as expected. The amplitude of temperature distortion, $\Delta T_{ef,\,max}$, is however more significant. In the glazed ice case with the heated wall and flight Mach number of 0.85, we note that the maximum temperature distortion amplitude reaches ~87 K (or ^{o}C) level, which is equivalent to ~156 ^{o}R (or ^{o}F). This shows higher amplitude for temperature distortion than the engine tests reported in Figure 2. However, we realize that the angular extent of the temperature distortion at the engine face in the S-duct is a fraction of the simulated tests at NASA. Consequently, we do not expect the same level of stall pressure degradation with temperature distortions in the S-duct as compared to engine tests in Figure 2. But these amplitudes are significant enough to warrant additional studies in inlet icing with heated walls. Finally, as we suspected, there is coupling between the heated wall boundary condition and the total pressure distortion in glaze ice case at flight Mach number of 0.85. We note that from

Table 4 where all distortion parameters, total pressure recovery, DC(60), DP and TD all suffer as a result of wall heating compared to the adiabatic wall boundary condition. For example, distortion parameter, DP, is increased by ~ 7% and distortion coefficient, DC(60), rises by 4.2% and temperature distortion is increased by 67% when the wall is heated to T_w=350 K.

Table 3 Distortion parameters at the engine face (clean)

(a) $M_\infty = 0.475$

Distortion Factors	Adiabatic wall	T_W=350 K	Increment (%)
Total pressure recovery	0.9469	0.9459	-0.11
DC(60)	0.6643	0.6314	-4.95
DP	0.1796	0.1846	2.78
$\Delta T_{ef,max}$ (K)	14.77	62.4	322.48
TD	0.0582	0.2424	316.49

(b) $M_\infty = 0.85$

Distortion Factors	Adiabatic wall	T_W=350 K	Increment (%)
Total pressure recovery	0.7888	0.7914	0.33
DC(60)	1.0677	1.0650	-0.25
DP	0.7354	0.7418	0.87
$\Delta T_{ef,max}$ (K)	62.8	73.34	16.78
TD	0.2914	0.3321	13.97

Table 4 Distortion parameters at the engine face (glaze)

(a) $M_\infty = 0.475$

Distortion Factors	Adiabatic wall	T_W=350 K	Increment (%)
Total pressure recovery	0.8356	0.8344	-0.14
DC(60)	0.3696	0.3772	2.06
DP	0.2597	0.2601	0.15
$\Delta T_{ef,max}$ (K)	17.07	46.33	171.41
TD	0.0659	0.1745	164.80

(b) $M_\infty = 0.85$

Distortion Factors	Adiabatic wall	T_W=350 K	Increment (%)
Total pressure recovery	0.6104	0.6073	-0.51
DC(60)	0.8018	0.8358	4.24
DP	0.9028	0.9657	6.97
$\Delta T_{ef,max}$ (K)	50.25	86.59	72.32
TD	0.2165	0.3618	67.11

CONCLUSION

The conclusion is that the temperature distortion in S-duct inlets with icing effects is real and significant. The flight Mach number and heated wall exacerbate the distortion levels at the engine face. Also, temperature distortion couples with total pressure distortion to create a higher engine face distortion level that may lead to compressor stall or engine surge. The amplitude of temperature distortion in glazed ice accretion case at high subsonic flight Mach number is large and may adversely affect the compressor stall margin. Additional effects of unsteadiness and asymmetry in ice formations need to be considered in future studies. Also, freestream turbulence level, Tu_∞, has a pronounced effect in mixing and thus the size of separation zones. Therefore, future studies should include the effect of freestream turbulence as well.

ACKNOWLEDGEMENT

REFERENCES

[1] Burcham, F. W., Jr., Calogeras, J. E., Meyer, C. L., Povolny, J. H., and Rudey, R. A., "Effects of Engine Inlet Disturbances on Engine Stall Performance," Paper in NASA-SP 259, Aircraft Propulsion, pp. 313-341, 1971.

[2] Farokhi, S, *Aircraft Propulsion,* John Wiley & Sons, Inc., New York, 2008.

[3] Seddon, J. and Goldsmith, E.L., *Intake Aerodynamics,* AIAA Education Series, AIAA, Washington, D.C., 1985.

[4] Potapczuk, M. G., "Numerical Analysis of an NACA 0012 Airfoil with Leading-Edge Ice Accretion," *Journal of Aircraft*, Vol. 25, No. 3, pp. 193-194, Mar. 1988.

[5] Bragg, M. B., Khodadoust, A., and Spring, S. A., "Measurement in a Leading-Edge Separation Bubble due to a Simulated Airfoil Ice Accretion," *AIAA Journal*, Vol. 30, No. 6, pp. 1462-1467, 1992.

[6] Kerho, M. F and Bragg, M. B., "Airfoil Boundary-Layer Development and Transition with Large Leading-Edge Roughness," *AIAA Journal* Vol. 35, No. 1, Jan. 1997.

[7] Kim, H. S. and Bragg, M. B., "Effects of Leading –Edge Ice Accretion Geometry on Airfoil Performance," AIAA Paper 99-3150. Jun. 1999.

[8] Chung, J., Choo, Y., Reehorst, A. L., Potapczuk, M. G., and Slater, J., "Navier-Stokes Analysis of the Flowfield Characteristics of and Ice Contaminated Aircraft Wing," AIAA Paper 99-0375, Jan. 1999.

[9] Henry, R., Guffond, D., Aschettino, S., and Duprat, G., "Characterization of Ice Roughness and Influence on Aerodynamic Performance of Simulated Ice Shapes," AIAA Paper 2001-0092, Jan. 2001.

[10] Jin, W. and Taghavi, R. R., "Computational Study of Icing Effects on the M2129 S-Duct Inlet," AIAA Paper 08-0075, Jan. 2008.

[11] Star-CCM+ Software Package, Ver. 2.10.013, CD-adapco Inc., Melville, NY, 2007.

[12] AGARD FTP Working Group 13, "Air Intakes for High Speed Vehicles," AR.270, Sept. 1991.

[13] Menzies, R. D. D., Babcock, K. J., Barakos, G. N., and Richards, B. E., "Validation of the Simulation of Flow in an S-duct," AIAA Paper 2002-2808, Jun. 2002.

[14] May, N. E., "A New Vortex Generator Model for Use in Complex Configuration CFD Solvers," AIAA Paper 2001-2434, Jun. 2002.

[15] Berrier, B. L. and Allan B. G., "Experimental and Computational Evaluation of Flush-Mounted, S-Duct Inlets," AIAA Paper 2004-764, Jan. 2004.

[16] Mohler, S. R. Jr., "WIND-US Flow Calculations for the M2129 S-Duct Using Structured and Unstructured Grids," AIAA Paper 2004-525, Jan. 2004.

[17] Anderson, B.H. and Farokhi, S., "A Study of Three-Dimensional Turbulent Boundary Layer Separation and Vortex Flow Control Using the Reduced Navier Stokes Equations," Turbulent Shear Flow Symposium, Munich, Germany, Sept. 1991.

[18] Bidwell, C. S., and Mohler, S. R., " Collection Efficiency and Ice Accretion Calculations for a Sphere, a Swept MS(1)-317 Wing, a Swept NACA-0012 Wing Tip, an Axisymmetric Inlet, and a Boeing 737-300 Inlet," NASA TM-106831, 1995.

[19] GAMBIT software Package, Ver. 2.2.30, Fluent Inc. Lebanon, NH, 2004.